

# Modified Martin-Puplett interferometer for magneto-optical Kerr effect measurements at sub-THz frequencies

Cite as: Rev. Sci. Instrum. 95, 113907 (2024); doi: 10.1063/5.0231004

Submitted: 27 July 2024 • Accepted: 30 October 2024 •

Published Online: 26 November 2024



View Online



Export Citation



CrossMark

A. Glezer Moshe,<sup>1,a</sup> R. Nagarajan,<sup>1</sup> U. Nagel,<sup>1</sup> T. Rõõm,<sup>1,b</sup> and G. Blumberg<sup>1,2,c</sup>

## AFFILIATIONS

<sup>1</sup> National Institute of Chemical Physics and Biophysics, Akadeemia tee 23, 12618 Tallinn, Estonia

<sup>2</sup> Department of Physics and Astronomy, Rutgers University, Piscataway, New Jersey 08854, USA

<sup>a</sup>Electronic mail: [aviv.glezer@kbf.ee](mailto:aviv.glezer@kbf.ee)

<sup>b</sup>Electronic mail: [toomas.room@kbf.ee](mailto:toomas.room@kbf.ee)

<sup>c</sup>Author to whom correspondence should be addressed: [girsh@physics.rutgers.edu](mailto:girsh@physics.rutgers.edu)

## ABSTRACT

We present a magneto-optical Kerr effect (MOKE) spectrometer based on a modified Martin-Puplett interferometer, utilizing continuous wave sub-THz low-power radiation in a broad frequency range. This spectrometer is capable of measuring the frequency dependence of the MOKE response function, both the Kerr rotation and ellipticity, simultaneously, with accuracy limited by a sub-milliradian threshold, without the need for a reference measurement. The instrument's versatility allows it to be coupled to a cryostat with optical windows, enabling studies of a variety of quantum materials such as unconventional superconductors, two-dimensional electron gas systems, quantum magnets, and other systems showing optical Hall response at sub-Kelvin temperatures and in high magnetic fields. We demonstrate the functionality of the MOKE spectrometer using an undoped InSb wafer as a test sample.

Published under an exclusive license by AIP Publishing. <https://doi.org/10.1063/5.0231004>

## I. INTRODUCTION

The application of a magnetic field can significantly alter the properties of materials. It is well-accepted that magneto-resistivity and Hall-effect measurements provide more comprehensive information compared to standard dc zero-field transport measurements. Similarly, the magneto-optical response carries new data about physical systems.<sup>1,2</sup>

Recent advancements in magneto-optical techniques have allowed for the acquisition of novel information about electronic systems by extending dc Hall conductivity measurements into the THz frequency range.<sup>3</sup> This spectroscopic approach is designed to complement transport experiments, testing the bounds of standard relaxation time approximation in metals,<sup>4</sup> measuring intrinsic Berry-phase contributions to the anomalous Hall effect, and probing mechanisms of spontaneous time-reversal symmetry breaking.<sup>5-7</sup> Electronic systems where magneto-optical spectroscopy has recently proven to be particularly informative are unconventional superconductors,<sup>8,9</sup> integer and fractional quantum

Hall systems,<sup>10,11</sup> quantum anomalous Hall states,<sup>12</sup> graphene-like systems,<sup>13</sup> magnetic topological insulators,<sup>14,15</sup> valley Hall effect 2D crystals,<sup>16</sup> and “strange metals,” including cuprates and heavy fermions near antiferromagnetic quantum critical points,<sup>4</sup> to name a few.

Magnetic fields induce non-reciprocal optical phenomena, such as the Faraday and Kerr rotations. These magneto-optical rotations play a pivotal role in characterizing quantum materials. An example of a notable area of recent interest is chiral superconductors, which possess non-trivial topological properties and order parameters that spontaneously break time-reversal symmetry (TRS).<sup>17,18</sup>

One of the greatest challenges in identifying superconductors that spontaneously break TRS is the limited availability of suitable probes.<sup>19</sup> Optical measurements of the polar Kerr effect (PKE), where the rotation angle of linearly polarized radiation reflected from a sample’s surface is detected, have emerged as a key method for identifying TRS-broken states in unconventional materials.<sup>20</sup> The Kerr rotation arises from the ac Hall conductivity in dimensions

perpendicular to the light's wave vector. For this Hall conductivity to be finite, the medium must break time-reversal symmetry and mirror symmetries about all planes parallel to the wave vector.<sup>6,7</sup> The detection of non-vanishing PKE polarization rotation at zero external magnetic field provides unambiguous evidence for finite anomalous ac Hall conductivity, thus indicating TRS-breaking.<sup>7,21–23</sup>

To distinguish the signature of broken TRS from effects due to natural optical activity, it is critical to measure the Kerr rotation angle rather than the Faraday rotation. This distinction is necessary because PKE is absent if TRS is preserved.<sup>5,7</sup>

Although recent PKE studies using a telecom laser at approximately a micrometer wavelength have identified spontaneous Kerr responses in several unconventional superconductors, such as  $\text{UPt}_3$ ,<sup>24</sup>  $\text{URu}_2\text{Si}_2$ ,<sup>25</sup>  $\text{PrOs}_4\text{Sb}_{12}$ ,<sup>9</sup>  $\text{UTe}_2$ ,<sup>26</sup> and  $\text{FeTe}_{0.55}\text{Se}_{0.45}$ ,<sup>27</sup> a significant limitation of these experiments is their restriction to a single near-visible radiation frequency. This frequency far exceeds the energy scale relevant to unconventional superconductivity, typically around 0.1 THz. Consequently, these results have sparked considerable debates regarding their interpretation. Key questions include whether the observed effects are intrinsic bulk properties of the superconductor or influenced by external factors such as pinned vortices<sup>28,29</sup> or inhomogeneities of the sample. More importantly, the microscopic origin and quantitative understanding of the TRS-broken state remain contentious issues that can only be resolved through ultra-low-frequency spectroscopic measurements of the Kerr response as a function of frequency, within the range relevant to superconductivity and magnetism that causes TRS-breaking. This necessitates a new generation of spectroscopic THz-range magneto-optical Kerr effect (MOKE) instruments.

There are very few MOKE instruments operating in the THz range. Shimano *et al.*<sup>30,31</sup> used a time-domain THz setup to measure the amplitude of reflected radiation with an angle of incidence of  $45^\circ$  in a 0.48 T magnetic field at room temperature, achieving an accuracy of about 10 mrad between 0.5 and 2.5 THz. The setup of Drew *et al.*<sup>32,33</sup> employs a  $\text{CO}_2$  laser to generate THz radiation at selected frequencies of 0.7, 1.3, and 2.5 THz. Using a rapidly rotating waveplate, the Faraday rotation angle can be measured with a resolution of about 0.1 mrad in transmission, and the Kerr rotation angle can be measured with a resolution of about 1 mrad in reflection. In time-domain methods, it is possible to separate Kerr and Faraday effects by isolating the Faraday rotation from the first pulse and subtracting it from the reflected pulse that travels twice through the sample and arrives later in time. The most recent time-domain setup, which employs dual detectors, reports a Faraday angle precision of about 0.02 mrad.<sup>34</sup> The challenges of THz-range ellipsometry are comprehensively discussed elsewhere.<sup>35</sup>

The previously described methods either use high-power radiation or are limited in the selection and resolution of frequencies. High-power radiation is highly detrimental for studying samples at sub-Kelvin temperatures, necessitating a new approach.

We have developed a MOKE spectrometer that uses very low incident power on the sample, about  $0.1\text{--}1\ \mu\text{W}$ , in the range of 0.1–1 THz to simultaneously measure both the real and imaginary parts of the Kerr response function, with accuracy limited by a sub-milliradian threshold. Below, we explain the underlying principle of the interferometer-based approach and demonstrate the performance of the instrument using MOKE measurement on an InSb semiconductor as a test sample.

## II. POLAR KERR EFFECT

### A. Reflection matrix transformation

Here, we analyze the state of initially linearly polarized radiation after reflection under normal incidence from a material where the normal modes of electromagnetic radiation propagation are circularly polarized. The relation between linearly polarized radiation,  $\mathbf{E} = (E_x, E_y)$ , and circularly polarized radiation propagating along the  $z$  axis is

$$(E_-, E_+) = \hat{\mathbf{U}}(E_x, E_y), \quad (1)$$

where the transformation matrix is

$$\hat{\mathbf{U}} = \frac{1}{\sqrt{2}} \begin{pmatrix} 1 & -i \\ -1 & -i \end{pmatrix}. \quad (2)$$

The reflection coefficient from the material–vacuum interface is

$$\hat{\mathbf{r}} = \begin{pmatrix} r_- & 0 \\ 0 & r_+ \end{pmatrix}. \quad (3)$$

Using the complex indices of refraction for the right-handed ( $N_-$ ) and left-handed ( $N_+$ ) modes in the material, the reflection coefficients for the vacuum–material interface are

$$r_\pm = \frac{N_\pm - 1}{N_\pm + 1}. \quad (4)$$

The initially linearly polarized radiation  $\mathbf{E}^i$  after reflection is transformed into  $\mathbf{E}^f = (E_x^f, E_y^f)$ ,

$$\mathbf{E}^f = \begin{pmatrix} -1 & 0 \\ 0 & 1 \end{pmatrix} \hat{\mathbf{U}}^{-1} \hat{\mathbf{r}} \hat{\mathbf{U}} \mathbf{E}^i = \hat{\mathbf{r}}_{xy} \mathbf{E}^i, \quad (5)$$

where the matrix

$$\begin{pmatrix} -1 & 0 \\ 0 & 1 \end{pmatrix}$$

inverts the  $x$  axis of the coordinate frame. Such transformation of the coordinate frame also changes the handedness of the reflected radiation, which is defined relative to the propagation direction,

$$(E_+, E_-) = \hat{\mathbf{U}} \begin{pmatrix} -1 & 0 \\ 0 & 1 \end{pmatrix} \hat{\mathbf{U}}^{-1} (E_-, E_+). \quad (6)$$

From Eq. (5), we get the reflection matrix for the linearly polarized radiation,

$$\hat{\mathbf{r}}_{xy} = -\frac{1}{2} \begin{pmatrix} r_+ + r_- & i(r_+ - r_-) \\ i(r_+ - r_-) & -(r_+ + r_-) \end{pmatrix}. \quad (7)$$

### B. Kerr rotation and ellipticity

Let us assume the incident linearly polarized radiation is  $\mathbf{E}^i = (E_x^i, 0)$ . Then, the reflected radiation using Eq. (7) becomes

$$(E_x^f, E_y^f e^{i\theta}) = -\frac{E_x^i}{2} \begin{pmatrix} r_+ + r_- \\ i(r_+ - r_-) \end{pmatrix}, \quad (8)$$

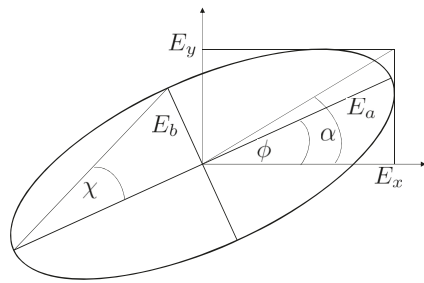


**FIG. 1.** Length of the ellipse's axes are  $E_a$  and  $E_b$ , and the major axis is rotated from the  $x$  axis by  $\phi$ . The electric field in the  $xy$  coordinate frame is  $(E_x, E_y e^{i\theta})$ , where  $E_x$  and  $E_y$  are the amplitudes and  $\theta$  is the phase difference between the components.

where  $\theta$  is the phase difference between the  $y$  and  $x$  components of the reflected radiation. We define the complex Kerr response function  $\Theta_K$  as

$$\Theta_K \equiv \Phi + iX = \frac{E_y^f}{E_x^f} e^{i\theta} = \frac{i(r_+ - r_-)}{r_+ + r_-}, \quad (9)$$

where the last equality comes from (8).  $\Phi$  and  $X$  are the real and imaginary parts of  $\Theta_K$ . With (9) the reflection matrix (7) for the linearly polarized radiation reads

$$\hat{\mathbf{t}}_{xy} = -\frac{r_+ + r_-}{2} \begin{pmatrix} 1 & \Theta_K \\ \Theta_K & -1 \end{pmatrix}. \quad (10)$$

The prefactor  $(r_+ + r_-)/2 = -E_x^f/E_x^i$  is the complex reflection coefficient for the linearly polarized radiation.

The Kerr response function  $\Theta_K$  is related to the rotation and ellipticity of radiation as follows: An elliptically polarized radiation,  $[E_x, E_y \exp(i\theta)]$ , is characterized by two parameters, the phase difference  $\theta$ , and the ratio of two orthogonal amplitudes,  $\tan \alpha = E_y/E_x$ . With this notation,

$$\Theta_K = \tan \alpha (\cos \theta + i \sin \theta). \quad (11)$$

The elliptically polarized state can be transformed into a coordinate frame where the phase difference between two orthogonal components is  $\pi/2$ ,  $\mathbf{E} = [E_a, E_b \exp(i\pi/2)]$ ; see Fig. 1. The rotation of

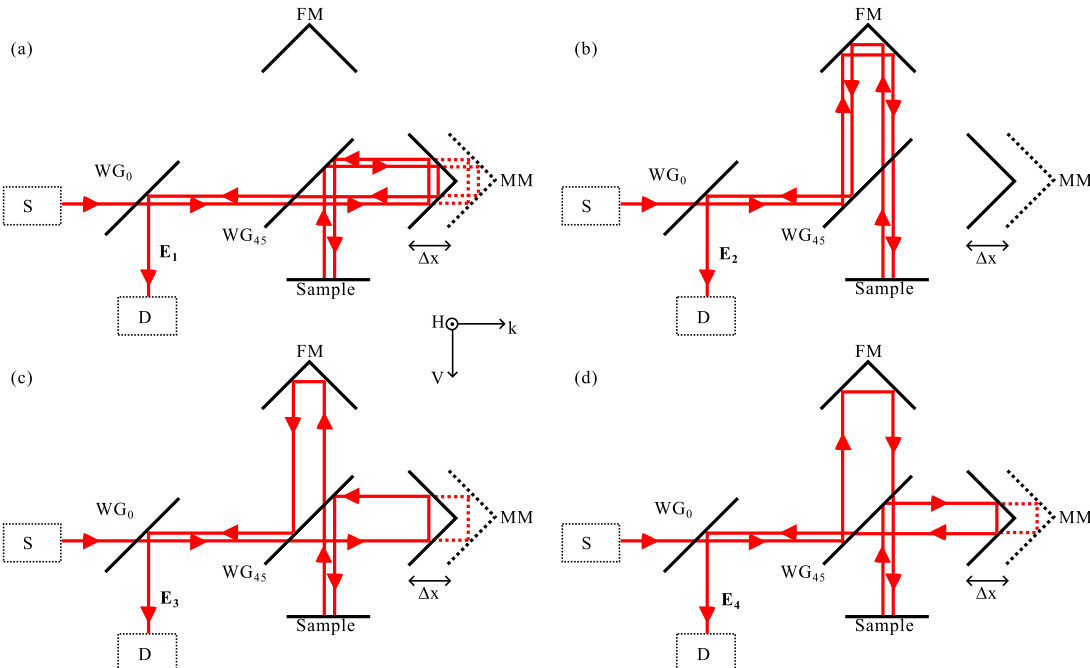


**FIG. 2.** Schematic of the MOKE interferometer and the radiation path through the MPI described in Eq. (16). The coordinate axis in the figure is in the frame of reference of the radiation beam emitted from the source.  $H$  and  $V$  refer to the horizontal and vertical directions of polarization of radiation propagating along  $\mathbf{k}$ . The optical elements are source (S), detector (D), fixed roof top mirror (FM), and moving roof top mirror (MM).  $WG_\eta$  is the wiregrid polarizer with wires aligned at angle  $\eta$  with respect to the H-axis shown in the figure. The displacement of the MM is  $\Delta x$ , where  $\Delta x = 0$  is the MM position when it is at the same distance from the beam splitter  $WG_{45}$  as FM. The direction of wires in  $WG_{45}$  is  $\eta = 45^\circ$  when the beam is incident on the beam splitter from the left or from the top in the figure. For the beams incident on the beam splitter from the right or from the bottom,  $\eta = -45^\circ$ . The direction of the roof top mirror line is set to  $\eta = 0$ , as described by the Jones matrix in Table I. If the incident radiation has polarization at  $\pm 45^\circ$  relative to the roof line, the reflected radiation will be orthogonal to the incident radiation. (a) The radiation beam is reflected from MM to sample to MM, adding the path difference  $4\Delta x$ , as described by  $E_1$  in Eq. (16). (b) The radiation beam is reflected from FM to sample to FM, and the path difference for this beam is zero, as described by  $E_2$ . (c) and (d) The radiation beam is reflected from MM (FM) to sample to FM (MM), respectively, adding a path difference of  $2\Delta x$ , as described by  $E_3$  ( $E_4$ ).

the ellipse main axis from the  $x$  axis is  $\phi$ , and the ellipticity is  $\chi = \arctan(E_b/E_a)$ . Then, see, e.g.,<sup>36</sup> (p. 28),

$$\begin{aligned}\tan(2\phi) &= \tan(2\alpha)\cos\theta, \\ \sin(2\chi) &= \sin(2\alpha)\sin\theta.\end{aligned}\quad (12)$$

If the ratio of amplitudes is small,  $\alpha \ll 1$ , we get from (11) and (12) the relation between the rotation and the ellipticity of radiation and the real and imaginary parts of the Kerr response function,

$$\begin{aligned}\phi &= \alpha \cos\theta = \Phi, \\ \chi &= \alpha \sin\theta = X.\end{aligned}\quad (13)$$

Under the normal incidence reflection from the vacuum–material interface, Eq. (4), the Kerr response function, Eq. (9), depends on the material index of refraction as<sup>2</sup>

$$\Theta_K = \frac{i(N_+ - N_-)}{N_+ N_- - 1}. \quad (14)$$

In the small  $\alpha$  limit using (14) in (13) we recover Argyres's result for the Kerr rotation and ellipticity,<sup>37</sup>

$$\begin{aligned}\phi &= -\Im \frac{(N_+ - N_-)}{N_+ N_- - 1}, \\ \chi &= \Re \frac{(N_+ - N_-)}{N_+ N_- - 1}.\end{aligned}\quad (15)$$

### III. WORKING PRINCIPLE OF THE MOKE SPECTROMETER

#### A. The modified Martin-Puplett interferometer

A schematic of the polar MOKE spectrometer<sup>38</sup> is shown in Fig. 2. The central part of the spectrometer is a four-beam interferometer consisting of a wiregrid beam splitter  $WG_{45}$ , and two roof top mirrors: the fixed mirror (FM) and the moving mirror (MM), with

**TABLE I.** Jones matrices of wiregrid, roof top mirror, and back reflection from the sample exhibiting polar Kerr effect.  $\eta$  is the angle of wiregrid wires and roof top mirror roof line from the horizontal direction measured toward the vertical direction. Horizontally polarized fields have unit vectors  $\mathbf{e}_h = (1, 0)$ , and vertically polarized has  $\mathbf{e}_v = (0, 1)$  and the beam propagation direction is  $\mathbf{e}_k = \mathbf{e}_h \times \mathbf{e}_v$ . Sample reflection matrix is Eq. (10) where  $\tilde{r} = (r_+ + r_-)/2$  and the complex Kerr response function  $\Theta_K = \Phi + iX$ .

Optical element	Jones matrix	Symbol
WG reflection	$\begin{pmatrix} -\cos^2\eta & -\cos\eta\sin\eta \\ \cos\eta\sin\eta & \sin^2\eta \end{pmatrix}$	$WG_\eta^R$
WG transmission	$\begin{pmatrix} \sin^2\eta & -\cos\eta\sin\eta \\ -\cos\eta\sin\eta & \cos^2\eta \end{pmatrix}$	$WG_\eta^T$
Roof top mirror	$\begin{pmatrix} -\cos 2\eta & -\sin 2\eta \\ \sin 2\eta & -\cos 2\eta \end{pmatrix}$	$RM_\eta$
Sample reflection	$-\tilde{r} \begin{pmatrix} 1 & \Theta_K \\ \Theta_K & -1 \end{pmatrix}$	$R_\Theta$

optical elements layout similar to the Martin–Puplett interferometer (MPI).<sup>39</sup> To enable the polar Kerr spectroscopy under normal incidence, a sample is placed into one of the interferometer two ports, and the source and detector, separated by the wiregrid  $WG_0$ , are in the other port.<sup>40</sup>

The beam emitted from the source S after passing through the polarizer  $WG_0$  is vertically polarized,  $\mathbf{E}_0 = E_0(0, 1)$ . The beam splitter  $WG_{45}$  splits the beam into two orthogonally polarized beams. These two beams,  $\mathbf{E}_1$  and  $\mathbf{E}_2$ , after reflection from the sample, arrive at detector D as shown in Figs. 2(a) and 2(b). If the sample has a non-zero MOKE, the beam after the reflection from the sample is split again by the beam splitter  $WG_{45}$  and two additional beams,  $\mathbf{E}_3$  and  $\mathbf{E}_4$ , reach the detector D, Figs. 2(c) and 2(d). The wiregrid  $WG_0$  transmits the vertical polarization from the source into the interferometer and reflects the horizontal polarization from the interferometer output beam to the detector.

The four beams reaching the detector D are derived by applying the Jones matrices, Table I, to the source beam  $\mathbf{E}_0$ ,

$$\begin{aligned}\mathbf{E}_1 &= WG_0^R \cdot WG_{-45}^T \cdot MM \cdot WG_{-45}^R \cdot R_\Theta \cdot WG_{-45}^R \cdot MM \cdot WG_{45}^T \cdot WG_0^T \cdot E_0(0, 1) = -\frac{1}{2}E_0\tilde{r}e^{8i\pi\xi}(1, 0), \\ \mathbf{E}_2 &= WG_0^R \cdot WG_{45}^R \cdot FM \cdot WG_{-45}^T \cdot R_\Theta \cdot WG_{45}^T \cdot FM \cdot WG_{45}^R \cdot WG_0^T \cdot E_0(0, 1) = \frac{1}{2}E_0\tilde{r}(1, 0), \\ \mathbf{E}_3 &= WG_0^R \cdot WG_{45}^R \cdot FM \cdot WG_{-45}^T \cdot R_\Theta \cdot WG_{-45}^R \cdot MM \cdot WG_{45}^T \cdot WG_0^T \cdot E_0(0, 1) = -\frac{1}{2}E_0\tilde{r}e^{4i\pi\xi}\Theta_K(1, 0), \\ \mathbf{E}_4 &= WG_0^R \cdot WG_{-45}^T \cdot MM \cdot WG_{-45}^R \cdot R_\Theta \cdot WG_{45}^T \cdot FM \cdot WG_{45}^R \cdot WG_0^T \cdot E_0(0, 1) = -\frac{1}{2}E_0\tilde{r}e^{4i\pi\xi}\Theta_K(1, 0),\end{aligned}\quad (16)$$

where  $\xi = \Delta x/\lambda$  is the reduced path difference,  $\Delta x$  is the position of the moving mirror relative to the zero path difference (ZPD) position,  $\lambda$  is the wavelength, and  $\tilde{r} = (r_+ + r_-)/2$ . After adding up the four beams in Eq. (16), the electric field on the detector is

$$E(\xi) = E_0\tilde{r} \left[ \frac{1}{2} \left( 1 - e^{8i\pi\xi} \right) - e^{4i\pi\xi}\Theta_K \right]. \quad (17)$$

To demonstrate how the real and imaginary parts of  $\Theta_K$  affect the interferogram, we plot using Eq. (17) the normalized amplitude  $|E(\xi)/(E_0\tilde{r})|$  as a function of mirror displacement in Fig. 3. At  $\xi = 0$ , the incident radiation at the sample surface is linearly polarized parallel to the direction transmitted by  $WG_0$ , and radiation reaches the detector only if the plane of polarization is rotated upon back reflection from the sample ( $\phi \neq 0$ ): the real part of  $\Theta_K$  lifts the minima of the normalized amplitude. At  $\xi = 1/8$  or  $\xi = 3/8$ , we have

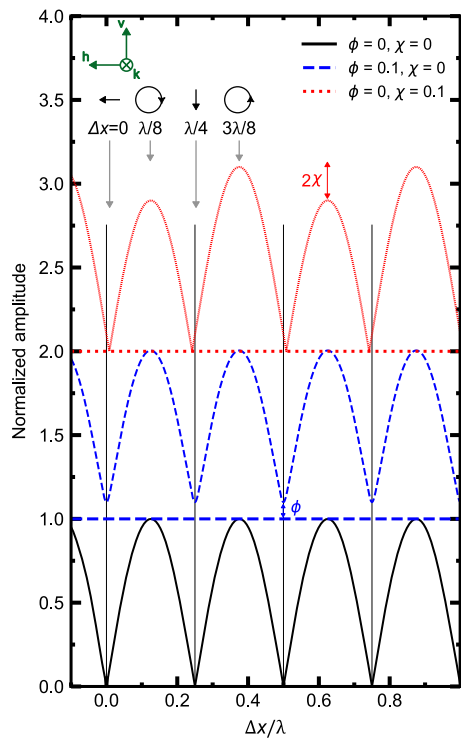


**FIG. 3.** Theoretical normalized electric field amplitude  $|E/E_0\bar{r}|$  at the detector calculated with Eq. (17) for different values of  $\Theta_K$ , arranged from bottom to top: zero rotation and zero ellipticity, finite rotation and zero ellipticity, and zero rotation and finite ellipticity, respectively. The values in the legend are given in units of radians. The curves are shifted by unity for clarity. It can be seen that the rotation lifts the minima by  $\phi$ , while the ellipticity separates the maxima by  $2\chi$ . Special points in the interferogram correspond to the polarization state of the incident radiation on the sample. At the maxima, the radiation is either left or right circularly polarized, while at the minima, the radiation is linearly polarized along the horizontal or vertical direction. The direction of rotation and polarization are shown along with the local coordinate system.

right- or left-handed circularly polarized radiation incident on the sample surface, and if an ellipticity  $\chi \neq 0$  is introduced by the sample, the maxima in the detected interferogram have different amplitudes. Finite ellipticity also shifts the positions of minima away from the position in the absence of ellipticity,  $\xi = n/4$ , where  $n = 0, 1, 2, \dots$

## B. Data analysis and accuracy

Following Eq. (17), we show that the normalized electric field intensity for the interferogram acquires a simple form, which is the sum of unmodulated rotation induced intensity  $\Phi^2$  and ellipticity induced baseline shift of interference modulation in the second intensity term,

$$I(\xi) = \left[ \frac{E(\xi)}{E_0\bar{r}} \right]^2 = \Phi^2 + [X + \sin(4\pi\xi)]^2. \quad (18)$$

A difference of intensity interferograms shifted by a quarter of the reduced path difference enables direct measurement of ellipticity  $X$  from the normalized intensity modulation amplitude,

$$I(\xi) - I\left(\xi - \frac{1}{4}\right) = 4X \sin(4\pi\xi). \quad (19)$$

Thus, one can obtain both the real and imaginary parts of the complex Kerr response function  $\Theta_K = \Phi + iX$  with insignificant cross correlation from the fit to measured interferogram amplitudes, Eq. (17), or intensities, Eqs. (18) and (19).

The figure of merit for MOKE measurements is the accuracy of Kerr rotation angle  $\delta\Phi$  and ellipticity  $\delta X$ . Below we first analyze the theoretical error propagation for the fitting procedure to Eqs. (17) and (18), assuming a normal distribution function for the radiation amplitude and the path difference position noise.<sup>41</sup>

We show below in Sec. IV A that the implemented data acquisition procedure readily achieves measured relative signal amplitude fluctuations  $\delta E_0/E_0$  better than  $5 \times 10^{-3}$ .<sup>42</sup> For the wavelength of interest, about a millimeter, commercially available high precision linear translation stages enable better than  $10^{-4}$  accuracy for the relative path difference control  $\delta\xi/\xi$ . With these parameters, a relatively quick interferogram measurement containing  $n = 200$  points per wavelength allows us to obtain relative ellipticity accuracy  $\frac{\delta X}{X} \propto \frac{\delta E_0}{E_0\sqrt{n}} \approx 0.35 \times 10^{-4}$ . Thus, small ellipticity can be quickly measured with sub-millirad accuracy, which can be further improved with the enhancement of measurement point density.

The situation is less favorable for the Kerr rotation angle accuracy  $\delta\Phi$  as this variable is not modulated by the interferogram scan; see Eq. (18). It appears that the relative Kerr rotation angle accuracy is inversely proportional to the square root of the number of points measured in the proximity of interferogram minima  $n_{\min}$ ,  $\frac{\delta\Phi}{\Phi} \propto \frac{\delta E_0}{E_0\sqrt{n_{\min}}}$ . Therefore, to obtain the Kerr rotation accuracy in the same order as the ellipticity accuracy, measurement with about an order of magnitude higher point density near the interferogram minima has to be implemented; see Sec. IV A. Experimentally, the point density is limited by the minimal repeatable incremental move distance of translational stages.<sup>43</sup>

Other contributions to the Kerr response function accuracy include photocurrent fluctuations in the Toptica detection system, interferences with intruding spurious back reflection beams from multiple surfaces of interferometer optical components, imbalance between two interferometer arms, frequency stability of the radiation, and non-orthogonality of the sample surface to the incoming beam, to name a few.

For example, the effect of imbalance between two interferometer arms, which remains present even after careful alignment of the optical components, results in a deviation from the ideal interferogram shape shown in Fig. 3, making the odd and even interferogram minima unequal; see Fig. 4. In practice, such an imbalance between two interferometer arms can be described by a modified interferometer electric field amplitude function

$$E(\xi) = E_0\bar{r} \left[ \frac{1}{2} \left( (1 - \delta)^2 - e^{8i\pi\xi} (1 + \delta)^2 \right) - e^{4i\pi\xi} \Theta_K (1 - \delta^2) \right], \quad (20)$$

where the electric field amplitude in the moving mirror arm is changed from the average of two by the factor  $1 + \delta$  and that of the fixed mirror arm by  $1 - \delta$ . Equation (20) introduces an additional, typically small, fitting parameter  $\delta$ ; see Fig. 4.

The relative signs of  $\delta$  and  $\Phi$  determine which of the two interferogram minima is smaller in amplitude. If the signs are opposite,

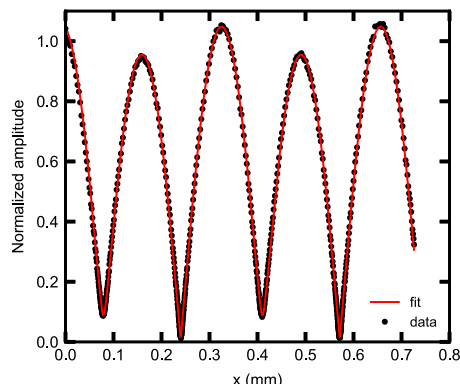


**FIG. 4.** An example of an interferogram used to determine the rotation  $\phi$  and ellipticity  $\chi$  measured from an undoped InSb semiconductor at  $T = 50$  K and magnetic field 5 mT. From the fit to Eq. (20), we obtained the rotation,  $\phi = 36 \pm 1$  mrad, ellipticity,  $\chi = 46.8 \pm 0.4$  mrad, and the frequency,  $452.45 \pm 0.07$  GHz. The radiation electric field amplitude and the data points were fitted to a model [Eq. (20)] that accounts for the imbalance between interferometer arms  $\delta = -0.0262 \pm 0.0006$ . To measure the locations of the minima, the path difference step size  $\Delta x$  was decreased linearly with decreasing amplitude down to  $0.10 \mu\text{m}$  from the initial value of  $3.37 \mu\text{m}$ . The 1 s integration time at maxima was increased as the inverse square root of the step size up to 5.7 s per interferogram point. This strategy allowed us to limit the total measurement time of the interferogram with 612 points to 33 min (including time for moving the roof mirror) while still having a relative amplitude error for each data point equal to about 0.5%.

then the even minima, including the one at ZPD, are deeper, and with the same signs of  $\delta$  and  $\Phi$ , the odd minima are deeper. Thus, knowing the ZPD position and following the signs of  $\delta$  and  $\Phi$  across the spectrum, we may obtain information about the sign of  $\Phi$ .<sup>44</sup>

We also note that  $\Theta_K(\omega) = \Phi(\omega) + iX(\omega)$  is a spectroscopic response function for which the real and imaginary parts are related by the Kramers–Kronig relations. Here,  $\omega$  is the radiation frequency. Thus, spectroscopic measurement of frequency dependence of ellipticity,  $X(\omega)$ , which is faster than the direct Kerr angle  $\Phi(\omega)$  measurement, may also give an estimate for the Kerr angle frequency dependence.

#### IV. SPECTROMETER AND PERFORMANCE TEST

##### A. Details of the MOKE spectrometer

The MOKE spectrometer is comprised of three units: the radiation source, the modified MP interferometer, and the detector of interfered four beams.

The optics assemblies for source and detector units are similar to each other; these are designed to (i) collimate the incoming beam from transmitter  $T_X$  and focus the outgoing beam on the receiver  $R_X$ , and (ii) isolate spurious back reflections from re-entering into the interferometer; **Fig. 5**.

The Optica Terascan 780 frequency domain THz spectroscopy system with GaAs photomixers coupled to log-spiral antennas is used to generate and detect the continuous-wave (cw) THz radiation. A voltage of about 10 V is applied in the  $T_X$  to accelerate the charge carriers to generate tunable circularly polarized 0.1–1 THz radiation at the beat frequency of the two distributed feedback

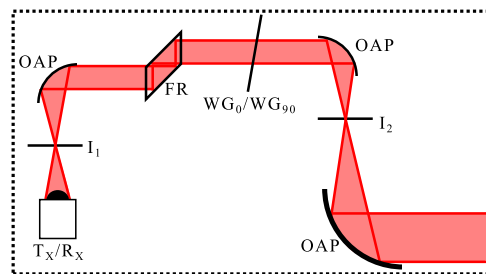


**FIG. 5.** Coupling of the transmitter/receiver ( $T_X/R_X$ ) to the modified MPI. OAP and  $I$  are off-axis parabolic mirrors and iris apertures of the spatial filters to collimate the beam. The Fresnel rhombs (FR) together with the output/input linear polarizers ( $WG_0/WG_{90}$ ) act as the broad band optical isolators of the source/detector units.

lasers.<sup>45–47</sup> We detect the photocurrent from  $R_X$  that is resulting from accelerating the charge carriers by the THz radiation.

An additional phase modulation extension, using two fiber stretchers, modulates the relative phase of laser radiation reaching the  $T_X$  and  $R_X$ , enabling simultaneous detection of the amplitude and phase of the THz radiation.<sup>48</sup> During a typical interferogram measurement time of about 30 min for 600 data points, the amplitude drifts less than 0.5%. The THz radiation frequency may drift over the interferogram measurement time: at 300 GHz, a typical frequency error from the fits is less than 0.08 GHz. The signal to noise ratio of detecting THz radiation amplitude depends on the integration time of the lockin detection at fiber stretcher frequency, where we typically reach more than two orders of magnitude in detecting the THz electric field amplitude. A comparable signal to noise ratio is not achievable with bolometric detection, where intensity (amplitude squared) is being measured.

Time-domain THz systems also measure the THz radiation amplitude, but they have a high THz radiation power on the sample surface. The advantage of a time-domain system as compared to a cw THz system is that it can separate the Fabry–Perot reflections from the main signal, although at the cost of reduced spectral resolution.

To suppress back reflections into the interferometer, we use broad band optical isolators in the source/detector units, comprising a linear polarizer and a Fresnel rhomb; see **Fig. 5**. The Fresnel rhombs convert the polarization of radiation from circular/linear to linear/circular at the output/input of  $T_X/R_X$  so that the back reflected radiation from  $T_X/R_X$  has orthogonal polarization with respect to the original beam and, therefore, is reflected away from the interferometer by the linear polarizer  $WG_0/WG_{90}$ . We designed and made the rhombs from TOPAS cyclic olefin copolymer<sup>49</sup> with non-parallel facets to avoid Fabry–Perot modulation within the rhombs. With this, we suppress the back reflections from  $T_X/R_X$  by more than an order of magnitude to less than 1% level. The parallel THz beam incident on the Fresnel rhomb facet has 1 in. diameter, while the beam is expanded to 2 in. diameter for the modified MP interferometer.

We use wiregrid (WG) polarization beam-splitters from Specac, which are made of 5  $\mu\text{m}$  diameter tungsten wires with a periodicity of 12.5  $\mu\text{m}$  and have close to ideal transmittance and reflectance characteristics.<sup>50</sup> At 0.3 THz, we measured better

than a 1:100 contrast in radiation amplitude between parallel and perpendicular polarized beams.

The hollow rooftop mirrors consist of two perpendicular (to 5 arc seconds accuracy) flat, unprotected Au-coated mirrors,<sup>51</sup> with the roof line aligned parallel to the H axis of the incident radiation beam, Fig. 2. The bare gold coating of 150 nm is sufficient for the frequency range of interest.

A 12 mm long translation stage<sup>52</sup> with a calculated 29 nm resolution of the actuator and minimal repeatable incremental movement of 0.2  $\mu\text{m}$  was used to move the rooftop mirror to control the path difference in the modified MPI.

## B. Performance test

As was first shown by Feil and Haas,<sup>53</sup> the dispersion of the diagonal part of the dielectric constant near the plasma frequency resonance in a metallic system has a strong influence on the MOKE properties. The plasma edge leads to resonance-like peaks in the Kerr rotation and ellipticity spectra with strong enhancement of the MOKE magnitude. This prediction was verified for InAs by Shimano *et al.*<sup>30</sup> at room temperature using a 0.48 T permanent magnet.

To test the performance of the MOKE spectrometer, we carried out MOKE measurements from a small direct gap undoped InSb semiconductor, which upon cooling to 50 K has a low plasma frequency of 0.5 THz and high mobility,  $\mu = 3 \times 10^5 \text{ cm}^2 \text{ V}^{-1} \text{ s}^{-1}$ . The small effective mass of charge carriers in InSb,  $m^* = 0.014m_e$ , guarantees high cyclotron frequency  $\omega_c = eB/m^*$  even for relatively low magnetic field  $B$ . Thus, the necessary condition of electron orbit coherence  $\omega_c\tau > 1$  ( $\tau$  is the mean free collision time) can be reached easily even in a few mT fields. For this system, Kerr rotation and ellipticity near the plasma frequency reach 100 mrad already at 5 mT field.

Under an external magnetic field perpendicular to the sample surface,  $\mathbf{B} \parallel \mathbf{z}$ , the optical conductivity tensor is<sup>37</sup>

$$\hat{\sigma} = \begin{pmatrix} \sigma_{xx} & \sigma_{xy} \\ -\sigma_{xy} & \sigma_{xx} \end{pmatrix}. \quad (21)$$

Within Drude approximation, the components of  $\hat{\sigma}$  are

$$\sigma_{xx} = \epsilon_0 \epsilon_b \omega_p^2 \frac{\gamma - i\omega}{(\gamma - i\omega)^2 + \omega_c^2}, \quad (22a)$$

$$\sigma_{xy} = -\epsilon_0 \epsilon_b \omega_p^2 \frac{\omega_c}{(\gamma - i\omega)^2 + \omega_c^2}, \quad (22b)$$

where  $\omega_p = \sqrt{n e^2 / m^* \epsilon_0 \epsilon_b}$  is the plasma frequency,  $n$  is the carrier density,  $e$  is the electron charge,  $\epsilon_0 = 8.85 \times 10^{-12} \text{ F m}^{-1}$  is the vacuum permittivity,  $\epsilon_b = 15.68$  is the background dielectric constant for InSb,<sup>54</sup> and  $\gamma = 1/\tau$  is the scattering rate. In this case, it is convenient to work in a circularly polarized radiation basis Eq. (1), where the index of refraction  $N$  depends on the handedness of radiation,

$$N_{\mp} = \sqrt{\epsilon_{xx} \pm i\epsilon_{xy}}, \quad (23a)$$

$$\epsilon_{xx} = \epsilon_b + i \frac{\sigma_{xx}}{\omega \epsilon_0}, \quad (23b)$$

$$\epsilon_{xy} = i \frac{\sigma_{xy}}{\omega \epsilon_0}, \quad (23c)$$

where we assumed  $\mu = 1$  for the magnetic permeability. Using Eqs. (14), (11), and (12), we obtain the frequency-dependent rotation  $\phi(\omega)$  and ellipticity  $\chi(\omega)$ . The three fitting parameters for the Drude model, Eq. (22), are  $\omega_p$ ,  $\omega_c$ , and  $\gamma$ .

As it is shown in Fig. 6, the frequency dependencies of the Kerr angle rotation and ellipticity obtained by fits of the individual interferograms measured from an undoped InSb wafer at 50 K and the external magnetic field of 5 mT using the modified interferometer electric field amplitude function, Eq. (20), are in agreement with the Drude model prediction. The result demonstrates the instrument's ability to track the sign change. The ideal instrument, described by Eq. (17), would not yield any information about the sign of  $\phi$ , but a small unbalance between the interferometer arms, Eq. (20), gives some information about the sign. It can be seen that by fitting the ellipticity alone, the rotation is predicted quite well, thus proving the reliability of the measurement. The parameters obtained from the Drude fit are  $\tau = 2.38 \pm 0.07 \text{ ps}$ ,  $\omega_p/2\pi = 483.2 \pm 0.4 \text{ GHz}$ , and  $\omega_c/2\pi = 10.3 \pm 0.3 \text{ GHz}$ . Using the relation  $\mu = e\tau/m^*$ , the mobility of the sample is  $\mu = (2.99 \pm 0.07) \times 10^5 \text{ cm}^2 \text{ V}^{-1} \text{ s}^{-1}$ . These values are in line with time-domain THz spectroscopy (TDS) reflection measurements on undoped InSb<sup>54</sup> and with the dc transport measurements performed on a separate sample cut from the same InSb wafer.

In Fig. 7, we also show the rotation and ellipticity as a function of the magnetic field measured at  $T = 50 \text{ K}$  and at frequency  $\omega = 442 \text{ GHz}$ . The magnetic field dependence of the rotation and ellipticity was simultaneously fitted to the Drude model, Eq. (22). The obtained fitting parameters  $\tau = 2.40 \pm 0.02 \text{ ps}$  and  $\omega_p/2\pi = 476.1 \pm 0.4 \text{ GHz}$  are in agreement with those obtained from fitting the rotation and ellipticity as a function of frequency.

The residuals of  $\phi$  and  $\chi$  shown in Fig. 7 indicate that the overall resolution for tracking small changes of the rotation and ellipticity is

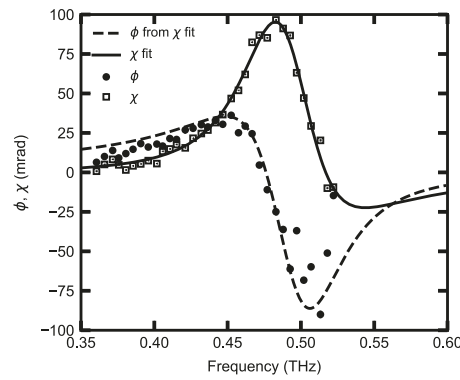


**FIG. 6.** Rotation  $\phi(\omega)$  and ellipticity  $\chi(\omega)$  spectra measured from undoped InSb at 50 K and in a magnetic field of 5 mT. To demonstrate the reliability of the measurement, we fitted the ellipticity  $\chi$  (full squares) to the Drude model (solid line) and plotted the theoretical rotation  $\phi$  (dashed line) using the fitting parameters obtained from the ellipticity fit. The fitting parameter  $\delta$  was in the range of  $-0.01$  to  $-0.05$ . The calculated rotation aligns well with the experimental data (full circles). The measurement time for each datapoint was 30 min.

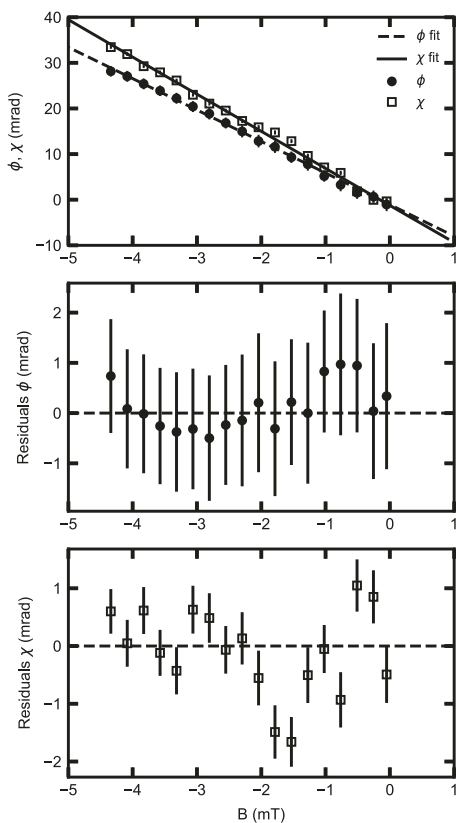


**FIG. 7.** Magnetic field dependence of rotation  $\phi$  and ellipticity  $\chi$  at 442.2 GHz and 50 K in undoped InSb. The dashed and solid lines are obtained by fitting simultaneously the magnetic field dependence of the rotation and ellipticity to the Drude model, Eq. (22). The measurement time for each datapoint was 30 min.

about 1 mrad at 442 GHz. A typical measurement time of an interferogram (Fig. 4) of 600 data points is 30 min, and the spacing of points near minima is determined by the precision of the moving mirror stage.

## V. SUMMARY

We have developed a MOKE spectrometer designed for simultaneous measurement of the Kerr rotation angle and ellipticity using continuous wave sub-THz low-power radiation over a broad frequency range under normal incidence to the sample, eliminating the need for reference measurements. We demonstrated that the spectrometer is capable of measuring the frequency dependence of the polar Kerr effect response function with accuracy limited by a sub-milliradian threshold.

The MOKE spectrometer is well-suited for integration with magneto-optical systems that have direct optical access. The implemented interferometric technique can be adapted to other radiation sources across a broad frequency range, including shorter wavelengths, by using polarizing beam splitter cubes. The instrument's versatility allows for the studies of magneto-optical effects in

quantum materials such as unconventional superconductors, two-dimensional electron gas systems, quantum magnets, and systems exhibiting the anomalous Hall effect at sub-Kelvin temperatures and in high magnetic fields.

## ACKNOWLEDGMENTS

The work was supported by the Estonian science agency Grant Nos. PRG736 and MOBJD1103 and by the European Research Council (ERC) under the European Union Horizon 2020 research and innovation program Grant Agreement No. 885413. The work at Rutgers was supported by the National Science Foundation (NSF) Grant No. DMR-2105001.

## AUTHOR DECLARATIONS

### Conflict of Interest

The authors have no conflicts to disclose.

### Author Contributions

**GB** conceived the project. **UN**, **GB**, and **TR** invented the measurement method. **TR**, **GB**, and **UN** modeled the response function of the interferometer. **UN**, **GB**, and **AGM** built the interferometer. **UN** created the LabVIEW code to run the Kerr interferometer and control the experiments. All authors performed the experiments and wrote the manuscript.

**A. Glezer Moshe:** Data curation (equal); Formal analysis (equal); Funding acquisition (equal); Investigation (equal); Methodology (equal); Validation (equal); Visualization (equal); Writing – original draft (equal). **R. Nagarajan:** Data curation (equal); Investigation (equal); Validation (equal); Writing – original draft (equal). **U. Nagel:** Conceptualization (equal); Data curation (equal); Formal analysis (equal); Funding acquisition (equal); Investigation (equal); Methodology (equal); Project administration (equal); Software (lead); Supervision (equal); Validation (equal); Visualization (equal); Writing – original draft (equal). **T. Rõõm:** Conceptualization (equal); Data curation (equal); Formal analysis (equal); Funding acquisition (equal); Investigation (equal); Methodology (equal); Project administration (equal); Supervision (equal); Validation (equal); Writing – original draft (equal). **G. Blumberg:** Conceptualization (equal); Data curation (equal); Formal analysis (equal); Funding acquisition (lead); Investigation (equal); Methodology (equal); Project administration (equal); Supervision (equal); Validation (equal); Writing – original draft (equal).

## DATA AVAILABILITY

The data that support the findings of this study are available from the corresponding author upon reasonable request.

## REFERENCES

1. A. Kimel, A. Zvezdin, S. Sharma, S. Shallcross, N. de Sousa, A. García-Martín, G. Salván, J. Hamrle, O. Stejskal, J. McCord, S. Tacchi, G. Carlotti, P. Gambardella, G. Salis, M. Münzenberg, M. Schultze, V. Temnov, I. V. Bychkov, L. N. Kotov, N. Maccaferri, D. Ignatyeva, V. Belotelov, C. Donnelly, A. H. Rodriguez, I. Matsuda, T. Ruchon, M. Fanciulli, M. Sacchi, C. R. Du, H. Wang, N. P. Armitage, M. Schubert, V. Darakchieva, B. Liu, Z. Huang, B. Ding, A. Berger, and P. Vavassori, "The 2022 magneto-optics roadmap," *J. Phys. D: Appl. Phys.* **55**, 463003 (2022).

<sup>2</sup>K. Sato and T. Ishibashi, "Fundamentals of magneto-optical spectroscopy," *Front. Phys.* **10**, 946515 (2022).

<sup>3</sup>J. Levallois, I. O. Nedoliuk, I. Crassee, and A. B. Kuzmenko, "Magneto-optical Kramers-Kronig analysis," *Rev. Sci. Instrum.* **86**, 033906 (2015).

<sup>4</sup>H. D. Drew and P. Coleman, "Sum rule for the optical Hall angle," *Phys. Rev. Lett.* **78**, 1572–1575 (1997).

<sup>5</sup>L. D. Landau, E. M. Lifshitz, and L. P. Pitaevskii, *Electrodynamics of Continuous Media* (Pergamon Press, 1984).

<sup>6</sup>B. I. Halperin, J. March-Russell, and F. Wilczek, "Consequences of time-reversal-symmetry violation in models of high- $T_c$  superconductors," *Phys. Rev. B* **40**, 8726–8744 (1989).

<sup>7</sup>W. Cho and S. A. Kivelson, "Necessity of time-reversal symmetry breaking for the polar Kerr effect in linear response," *Phys. Rev. Lett.* **116**, 093903 (2016).

<sup>8</sup>Z. Wang, J. Berlinsky, G. Zwicknagl, and C. Kallin, "Intrinsic ac anomalous Hall effect of nonsymmorphic chiral superconductors with an application to UPt<sub>3</sub>," *Phys. Rev. B* **96**, 174511 (2017).

<sup>9</sup>E. M. Levenson-Falk, E. R. Schemm, Y. Aoki, M. B. Maple, and A. Kapitulnik, "Polar Kerr effect from time-reversal symmetry breaking in the heavy-fermion superconductor PrOs<sub>4</sub>Sb<sub>12</sub>," *Phys. Rev. Lett.* **120**, 187004 (2018).

<sup>10</sup>Y. Ikebe, T. Morimoto, R. Masutomi, T. Okamoto, H. Aoki, and R. Shimano, "Optical Hall effect in the integer quantum Hall regime," *Phys. Rev. Lett.* **104**, 256802 (2010).

<sup>11</sup>V. Dzjom, A. Shubaev, A. V. Shchepetilnikov, D. MacFarland, G. Strasser, and A. Pimenov, "High-frequency breakdown of the integer quantum Hall effect in GaAs/AlGaAs heterojunctions," *Phys. Rev. B* **99**, 045305 (2019).

<sup>12</sup>K. N. Okada, Y. Takahashi, M. Mogi, R. Yoshimi, A. Tsukazaki, K. S. Takahashi, N. Ogawa, M. Kawasaki, and Y. Tokura, "Terahertz spectroscopy on Faraday and Kerr rotations in a quantum anomalous Hall state," *Nat. Commun.* **7**, 12245 (2016).

<sup>13</sup>V. P. Gusynin, S. G. Sharapov, and J. P. Carbotte, "Sum rules for the optical and Hall conductivity in graphene," *Phys. Rev. B* **75**, 165407 (2007).

<sup>14</sup>R. Yu, W. Zhang, H.-J. Zhang, S.-C. Zhang, X. Dai, and Z. Fang, "Quantized anomalous Hall effect in magnetic topological insulators," *Science* **329**, 61–64 (2010).

<sup>15</sup>C.-Z. Chang, J. Zhang, X. Feng, J. Shen, Z. Zhang, M. Guo, K. Li, Y. Ou, P. Wei, L.-L. Wang, Z.-Q. Ji, Y. Feng, S. Ji, X. Chen, J. Jia, X. Dai, Z. Fang, S.-C. Zhang, K. He, Y. Wang, L. Lu, X.-C. Ma, and Q.-K. Xue, "Experimental observation of the quantum anomalous Hall effect in a magnetic topological insulator," *Science* **340**, 167–170 (2013).

<sup>16</sup>K. F. Mak, K. L. McGill, J. Park, and P. L. McEuen, "The valley Hall effect in MoS<sub>2</sub> transistors," *Science* **344**, 1489–1492 (2014).

<sup>17</sup>C. Kallin and J. Berlinsky, "Chiral superconductors," *Rep. Prog. Phys.* **79**, 054502 (2016).

<sup>18</sup>M. Sato and Y. Ando, "Topological superconductors: A review," *Rep. Prog. Phys.* **80**, 076501 (2017).

<sup>19</sup>S. K. Ghosh, M. Smidman, T. Shang, J. F. Annett, A. D. Hillier, J. Quintanilla, and H. Yuan, "Recent progress on superconductors with time-reversal symmetry breaking," *J. Phys.: Condens. Matter* **33**, 033001 (2020).

<sup>20</sup>A. Kapitulnik, J. Xia, E. Schemm, and A. Palevski, "Polar Kerr effect as probe for time-reversal symmetry breaking in unconventional superconductors," *New J. Phys.* **11**, 055060 (2009).

<sup>21</sup>P. Brydon, D. Abergel, D. Agterberg, and V. M. Yakovenko, "Loop currents and anomalous Hall effect from time-reversal symmetry-breaking superconductivity on the honeycomb lattice," *Phys. Rev. X* **9**, 031025 (2019).

<sup>22</sup>A. Kapitulnik, "Notes on constraints for the observation of Polar Kerr effect in complex materials," *Physica B* **460**, 151–158 (2015), part of Special Issue: Special issue on Electronic Crystals (ECRYS-2014).

<sup>23</sup>N. P. Armitage, "Constraints on Jones transmission matrices from time-reversal invariance and discrete spatial symmetries," *Phys. Rev. B* **90**, 035135 (2014).

<sup>24</sup>E. R. Schemm, W. J. Gannon, C. M. Wishne, W. P. Halperin, and A. Kapitulnik, "Observation of broken time-reversal symmetry in the heavy-fermion superconductor UPt<sub>3</sub>," *Science* **345**, 190–193 (2014).

<sup>25</sup>E. R. Schemm, R. E. Baumbach, P. H. Tobash, F. Ronning, E. D. Bauer, and A. Kapitulnik, "Evidence for broken time-reversal symmetry in the superconducting phase of URu<sub>2</sub>Si<sub>2</sub>," *Phys. Rev. B* **91**, 140506 (2015); [arXiv:1410.1479](https://arxiv.org/abs/1410.1479).

<sup>26</sup>I. M. Hayes, D. S. Wei, T. Metz, J. Zhang, Y. S. Eo, S. Ran, S. R. Saha, J. Collini, N. P. Butch, D. F. Agterberg, A. Kapitulnik, and J. Paglione, "Multicomponent superconducting order parameter in UTe<sub>2</sub>," *Science* **373**, 797–801 (2021).

<sup>27</sup>C. Farhang, N. Zaki, J. Wang, G. Gu, P. D. Johnson, and J. Xia, "Revealing the origin of time-reversal symmetry breaking in Fe-chalcogenide superconductor FeTe<sub>1-x</sub>Se<sub>x</sub>," *Phys. Rev. Lett.* **130**, 046702 (2023).

<sup>28</sup>M. Ajeeesh, M. Bordelon, C. Girod, S. Mishra, F. Ronning, E. Bauer, B. Maiorov, J. Thompson, P. Rosa, and S. Thomas, "Fate of time-reversal symmetry breaking in UTe<sub>2</sub>," *Phys. Rev. X* **13**, 041019 (2023).

<sup>29</sup>N. Azari, M. Yakovlev, N. Rye, S. R. Dunsiger, S. Sundar, M. M. Bordelon, S. M. Thomas, J. D. Thompson, P. F. S. Rosa, and J. E. Sonier, "Absence of spontaneous magnetic fields due to time-reversal symmetry breaking in bulk superconducting UTe<sub>2</sub>," *Phys. Rev. Lett.* **131**, 226504 (2023).

<sup>30</sup>R. Shimano, Y. Ino, Y. P. Svirko, and M. Kuwata-Gonokami, "Terahertz frequency Hall measurement by magneto-optical Kerr spectroscopy in InAs," *Appl. Phys. Lett.* **81**, 199–201 (2002).

<sup>31</sup>Y. Ino, R. Shimano, Y. Svirko, and M. Kuwata-Gonokami, "Terahertz time domain magneto-optical ellipsometry in reflection geometry," *Phys. Rev. B* **70**, 155101 (2004).

<sup>32</sup>G. S. Jenkins, D. C. Schmadel, and H. D. Drew, "Simultaneous measurement of circular dichroism and Faraday rotation at terahertz frequencies utilizing electric field sensitive detection via polarization modulation," *Rev. Sci. Instrum.* **81**, 083903 (2010).

<sup>33</sup>G. S. Jenkins, A. B. Sushkov, D. C. Schmadel, N. P. Butch, P. Syers, J. Paglione, and H. D. Drew, "Terahertz Kerr and reflectivity measurements on the topological insulator Bi<sub>2</sub>Se<sub>3</sub>," *Phys. Rev. B* **82**, 125120 (2010).

<sup>34</sup>Z. Tagay, R. Romero, and N. P. Armitage, "High-precision measurements of terahertz polarization states with a fiber coupled time-domain THz spectrometer," *Opt. Express* **32**, 15946 (2024).

<sup>35</sup>M. Neshat and N. Armitage, "Developments in THz range ellipsometry," *J. Infrared, Millimeter, Terahertz Waves* **34**, 682–708 (2013).

<sup>36</sup>M. Born and E. Wolf, *Principles of Optics* (Cambridge University Press, 1999).

<sup>37</sup>P. N. Argyres, "Theory of the Faraday and Kerr effects in ferromagnetics," *Phys. Rev.* **97**, 334–345 (1955).

<sup>38</sup>G. Blumberg, T. Rööm, and U. Nagel, "Techniques for precise determination of the magneto-optic Kerr effect (MOKE) in materials in controlled environments," U.S. patent WO/2024/173475 (2024).

<sup>39</sup>D. Martin and E. Puplett, "Polarised interferometric spectrometry for the millimetre and submillimetre spectrum," *Infrared Phys.* **10**, 105–109 (1970).

<sup>40</sup>Interferometer arms are the ones with roof mirrors with the beam splitter in between. The modified MP interferometer has two symmetric ports on the other side of the beam splitter: Input and output. In a traditional MPI, the light is being sent from one port and the detection occurs at the second port after a single pass. In shown here polar MOKE spectrometer configuration, we direct light to pass through the interferometer a second time after reflection from the sample, as it is illustrated in Fig. 2

<sup>41</sup>The latter can be considered as the interferogram phase fluctuation noise

<sup>42</sup>This accuracy can be further improved by implementing an amplitude modulation measurement schema

<sup>43</sup>Stages with air bearing and interferometric position readout provide better positioning accuracy

<sup>44</sup>Additionally, the sign of  $\Phi$  could be obtained from the behavior of the phase of the detected signal. We have not used the phase information so far, because of too large overall phase drifts that are caused by THz frequency and optical setup instabilities, including the lasers and fibers that connect the lasers to the photomixers

<sup>45</sup>See <https://www.toptica.com/products/terahertz-systems/frequencydomain/terascan/> for technical details on the THz antennas.

<sup>46</sup>A. Roggenbuck, H. Schmitz, A. Deninger, I. C. Mayorga, J. Hemberger, R. Güsten, and M. Grüninger, "Coherent broadband continuous-wave terahertz spectroscopy on solid-state samples," *New J. Phys.* **12**, 043017 (2010).

<sup>47</sup>A. Roggenbuck, M. Langenbach, K. Thirunavukkurasu, H. Schmitz, A. Deninger, I. Cámara Mayorga, R. Güsten, J. Hemberger, and M. Grüninger, "Enhancing the stability of a continuous-wave terahertz system by photocurrent normalization," *J. Opt. Soc. Am. B* **30**, 1397–1401 (2013).

<sup>48</sup>A. Roggenbuck, K. Thirunavukkuarasu, H. Schmitz, J. Marx, A. Deninger, I. C. Mayorga, R. Güsten, J. Hemberger, and M. Grüninger, “Using a fiber stretcher as a fast phase modulator in a continuous wave terahertz spectrometer,” *J. Opt. Soc. Am. B* **29**, 614–620 (2012).

<sup>49</sup>See <https://topas.com/products/topas-coc-polymers/> for details on TOPAS polymers.

<sup>50</sup>M. Mičica, V. Bucko, K. Postava, M. Vanwolleghem, J.-F. Lampin, and J. Pištora, “Analysis of wire-grid polarisers in terahertz spectral range,” *J. Nanosci. Nanotechnol.* **16**, 7810–7813 (2016).

<sup>51</sup>See <https://www.plxinc.com/products/hollow-roof-mirrors-hrm/groups/rm202> for details on the roof mirror.

<sup>52</sup>See <https://www.thorlabs.com/thorproduct.cfm?partnumber=MT1/MZ8> for details on the motorized stage that controls the moving mirror position.

<sup>53</sup>H. Feil and C. Haas, “Magneto-optical Kerr effect, enhanced by the plasma resonance of charge carriers,” *Phys. Rev. Lett.* **58**, 65–68 (1987).

<sup>54</sup>S. C. Howells and L. A. Schlie, “Transient terahertz reflection spectroscopy of undoped InSb from 0.1 to 1.1 THz,” *Appl. Phys. Lett.* **69**, 550–552 (1996).